Final Technical Report

Title: Inversion and Prediction of Ground Motion of the 2009 L'Aquila Italy Mw 6.3 Earthquake

U.S.G.S Award Number G10AP00010
2010/1/1-2011/12/31

Chen Ji, Ralph Archuleta, Toshiro Tanimoto

University of California, Santa Barbara, California, 93106
Ph. (805) 893-2923; Fax (805)893-2314; ji@geol.ucsb.edu

Abstract

In view of significant discrepancy between the slip models of the April 6, 2009 L'Aquila, (Italy) earthquake based on seismic waveforms or geodetic data, a new inversion strategy is proposed to constrain the co-seismic rupture model and earlier post-seismic afterslip model of this earthquake simultaneously from the joint inversion of near-source strong ground motion recordings, P teleseismic body waves, Long period Rayleigh waves, GPS displacement vectors, and InSAR line of sight (LOS) displacement image. The fault is defined to strike 140° and dip 50° to the southwest. Co-seismic period here represents the first 10 s after the rupture initiation when over ninety-nine percent of our estimated co-seismic scalar moment of 3.07 X 10^{18} Nm occurred. Most co-seismic slip occurs in a small rupture area of approximately 16 km along strike and nearly 8 km in the dip direction, in a depth range of 4-10 km. The average slip is 0.45 m. The peak slip reaches about 0.90 m. Our result reveals that L'Aquila rupture has a lag of 0.6 s before it first propagates up-dip to break an Mw 5.7 asperity and then propagates along strike to break a large patch located 8 km along strike and 4 km up-dip from the hypocenter. The weighted average rise time and slip velocity are 0.71 s and 0.77 m/s, respectively. Our estimate of radiated seismic energy is 1.67×10^{13} J., yielding an energy to seismic moment ratio of 0.55×10^{-5}, considerably smaller than the global average for shallow earthquake (3×10^{-5}, [*Ide and Beroza*, 2001]). The earlier post-seismic period here mainly represents the time window from 10 s to the first day. Our result suggests that the accumulative afterslip during this period is 6.0×10^{17}Nm, equivalent to an Mw of 5.8. The afterslip concentrates near the vicinity of the patches with high co-seismic slip. For the fault plane deeper than 4 km, the earlier afterslip occurs next to the fault paths with significant later afterslip during a 180-day period after April 12, 2009 [*D'Agostino et al.*, 2012]. For the fault plane shallower than 4 km, the fault patches with earlier and later afterslip are overlapped.

Introduction

The April 6, 2009 Mw 6.3 L'Aquila earthquake occurred in the central Apennines (Abruzzo region) near the medieval town L'Aquila, Italy and led to 300 fatalities. This earthquake is the best-recorded Mw>6 normal-faulting event in terms of near-source strong motion observations. There were a total of 17 three-components strong-motion recordings within 50 km of the epicenter. Of these, 10 are within 20 km. Besides, the static deformation field associating with this earthquake was also captured by tens permanent and campaign GPS benchmarks operated by the Central Apennine Geodetic Network (CaCeoNet) and interferometic synthetic aperture radar (INSAR) images derived from ENVISAT and POLSAR images. The study of this earthquake shall improve our understanding to the continental normal faulting earthquakes.

In this research we have proposed a new inversion strategy to simultaneously constrain the co-seismic rupture model and earlier post-seismic afterslip model of the April 6, 2009 L'Aquila, (Italy) earthquake from the joint inversion of near-source strong ground motion recordings, P teleseismic body waves, Long period Rayleigh waves, GPS displacement vectors, and InSAR line of sight (LOS) displacement image. This was done after we observed significant discrepancy between the slip models based on seismic waveforms or geodetic data. We have also developed a 1D velocity structure for L'Aquila basin using the ZH ratio method developed recently [*T Yano et al.*, 2009] and the continuous broadband waveforms recorded by MEDNET station AQU during a 2 year period from 2006 to 2008. The results of this effort were reported at the 2009 American Geophysics Union (AGU) annual meeting [*T E Yano et al.*, 2009], 2010 Seismological Society of America (SSA) meeting [*T. E. Yano et al.*, 2010b], 2010 Earthquake Source Dynamics meeting [*T. E. Yano et al.*, 2010], and 2010 Southern California Earthquake Center annual meeting [*T. E. Yano et al.*, 2010a]. A manuscript is in preparation.

Approach

Precision of the inverted co-seismic slip distribution relies on the quality of observations, fault geometry, and earth structure. Our efforts then include:

1. In order to deal with the lateral heterogeneity of local velocity structure, we used two 1D velocity models to calculate the earth response inside and outside the L'Aquila basin. One of them is developed during this study.
2. In order to improve the constraint to the total seismic moment, we have combined the strong motion waveforms with the long period (133 s <Period< 266 s) Rayleigh waves.
3. The unwrapped InSAR LOS displacements usually include the errors caused by unwrapped data process, precision of baseline, atmosphere perturbation etc. We have developed a 2-step inversion strategy to simultaneously correct it during the finite fault inversion.
4. To deal with the inconsistence between the seismic data and geodetic data, we propose a new strategy to preform source inversion using multiple datasets. When there is large postseismic deformation recorded by the geodetic data, this approach

will not only resolve the co-seismic slip distribution but also estimate the postseismic rupture, even though we cannot directly separate the two fields from the geodetic observations.

Results

a) 1D velocity structure inside the L'Aquila basin

We have used two 1D velocity models to calculate the earth response inside and outside the L'Aquila basin. For the stations located outside the basin, we adopted the Bagh model [*Bagh et al.*, 2007] (blue line, Figure 2), which was developed as an average model for a 5000 km^2 area around the Central Apennines of Italy [*Bagh et al.*, 2007]. For the stations inside the basin, we have specially constrained a 1D velocity structure, hereafter referred as LVZ model, using the ZH ratio method developed recently [*T Yano et al.*, 2009]. Figure 2 shows the comparison of the two models. The LVZ model has a very slow near surface velocity (1.1 km/s). The ZH ratios are the ratios of vertical and horizontal particle motion of fundamental Rayleigh waves at different frequencies [*T Yano et al.*, 2009]. We estimate them using the continuous waveform records at MEDNET station AQU. Each dot in right side of Figure 2 represents the mean value of ZH ratios measured every hour during a two-year period from 2006 to 2008. Error bars associated with dots indicate one standard deviation from the mean. The measurements span a frequency range from 0.11 Hz to 0.40 Hz, which shall be sensitive to the average velocity structure within the depth range of top 10 km. Figure 2 compares the observed ZH ratios with the theoretical ZH ratios calculated using RF model, Bagh model, and LVZ model. It can be seen that Bagh model overestimates all ZH ratios measurements. The RF model could explain the measurements with relatively low frequency but fail to match the measurements for frequency larger than 0.25 Hz. Only the LVZ model is capable of explaining the ZH ratio measurements for the entire frequency band.

To illustrate the effects of using different velocity models, we have calculated synthetic seismograms and static displacements excited by a point source located at the hypocenter. Figure 3 compares the results of the Bagh model (in blue) with these of LVZ model (in red). The upper portion of Figure 3 compares the calculations of horizontal static displacements. It can be seen that using different velocity models not only affects the magnitudes of vectors but also their horizontal directions. The effects could be significant for the stations with relatively smaller horizontal amplitudes but large vertical amplitudes, e.g., the synthetics at GPS station ROIO. The lower portion of Figure 3 shows the comparison of velocity waveforms. To highlight the difference in waveforms, the synthetics have been aligned with the P-wave arrival times. It can be seen that for the station very close to the epicenter, such as station AGV, the synthetic waveforms of these two models are very similar, though the predictions using the LVZ model have larger amplitudes than these of Bagh model. For the distant records, the synthetic seismograms of LVZ model have much stronger reverberation with period from 2 to 3 s. Both of these discrepancies are consistent with the fact that LVZ model features a very low velocity in the top 2 km and the large velocity gradient from 2 to 8 km, which traps the seismic energy.

b) Model I: A slip model constrained by seismic-only

We first constrain a slip model using seismic data only. In this study, we have used 15 3-component velocity records, which have been bandpass filtered from 0.02 to 0.625 Hz. Although near-fault strong motion data set provides the highest sensitivity to the detailed spatiotemporal rupture history, these velocity waveforms are not very sensitive to the total seismic moment [*Shao and Ji,* 2012]. We overcome this limitation by further including teleseismic broadband body waves and long period surface waves. We selected 6 broadband P waves and 28 Rayleigh waves, which were bandpass filtered from 133 s to 266 s. A representative inversion result is shown in Figure 4a, hereafter refer it as Model I. The total seismic moment of Model I is 3.0×10^{18}Nm, which is 22% smaller than the GCMT solution (http://www.globalcmt.org). The centroid depth of Model I is only 7 km, 5 km shallower than that of GCMT solution (12 km). As the Rayleigh wave excitation generally becomes smaller as the depth increases [e.g., *Romanowicz and Guillemant*, 1984], the discrepancy in centroid depth might explain their difference in total seismic moment.

c) Model II: A slip model constrained by geodetic data only

We second constrain a slip model using geodetic data only. We have used 53 co-seismic GPS observations processed by *Cheloni* et al. [2010] and LOS displacement variation from April 27, 2008 to April 12, 2009. We have subsampled the SAR data before they are used to constrain the slip model using a script developed by [*Simons et al.*, 2002]. It is noteworthy that the LOS displacements reflect not only the ground deformation field but also the errors introduced during unwrapped process [Rosen et al., 2004], we have developed a scheme which could correct it simultaneously during the inversion of slip distribution. Figure 4b shows the slip model constrained using the geodetic data only, hereafter referred as Model II. Its total seismic moment is 3.7×10^{18}Nm, which is 23% larger than Model I. However, the centroid depth inferred from this model is 6.9 km, agreeing with Model I remarkably. The peak slip occurred in a depth of 5.6 km, 7 km away from the hypocenter in along strike direction and 4 km away in up-dip direction. The overall slip distribution is consistent with previous results based on geodetic data [e.g., *D'Agostino et al.*, 2012].

d) Simultaneously inverting co-seismic and post-seismic deformations by combined seismic and geodetic data together.

Regardless the overall consistence between the Model I and Model II, notable differences exist (Figure 4a and 4b). For instance, it can be seen that on the top 4 km of fault surface, the inverted slip is less than 20 cm in Model I (Figure 4a) but is up to 40 cm in Model II (Figure 4b). To illustrate the magnitude of discrepancy between these two models, Figure 5a shows the residuals by simply scalar subtracting the Model I from Model II. The residuals change from -0.26 m to 0.58 m. The large residuals (>0.5 m) are concentrated northwest of the hypocenter and the fault patch from 3 to 9 km along strike and 4 to 8 km downdip. Generally, the existence of residuals between the models constrained with

different data shall not be surprised. Each data has its spatial coverage to the source, which leads to its individual spatial resolution on the fault plane. In the fault patch where the slip cannot be fully constrained with one type of data, inversion regulations, such as the Laplace smoothing constraint mentioned above, step in and adjust the inverted slip distribution accordingly. Therefore, unless the spatial resolutions of different datasets are exactly same, the differences between inverted models are inevitable. However, considering the good strong motion station and geodetic coverage of the L'Aquila earthquake mentioned above, the residual amplitudes (up to 90% of the maximum slip in Model I and 60% in model II) shown in Figure 5a are too big to be entirely explained with this mechanism.

For 2009 L'Aquila earthquake the deformation field excited the observed seismic waves is not exactly same as the field that produced geodetic observations. The former occurred within a short time window of 10 s as suggested by the moment rate function (Figure 4d). In contrast, the GPS daily solutions included all deformations within the first day. Avallone et al. [2011] reported the notable differences between GPS daily solutions and what are inferred from the high rate GPS waveforms, which are presumably due to the post-seismic deformation. InSAR data reflects the pre-seismic deformation from April 27, 2008 and April 6, 2009 as well as the post-seismic deformation from April 6, 2009 to April 12, 2009. While the pre-seismic deformation might not be significant, the post-seismic deformation within the first a few days could be one of important causes of big residuals shown in Figure 6a.

For the convenience of discussion, we temporally divide the deformation field observed by geodetic data into two parts, "co-seismic" and "post-seismic". Here the "co-seismic" period is strictly defined based on seismic data, 10 s since the rupture nucleation in this study. However, the "post-seismic" deformation here is not exactly correct and shall include all deformations occurring before or after the "co-seismic" period defined above. We further assume that both of them occurred on the same fault plane. During the inversion, our target model is then composed of the slip on two identical fault planes. The slip on the first fault plane is to approximate the "co-seismic" deformation. So the slip could excite seismic waves and generate static deformation. The slip on the second plane is to model the "post-seismic" deformation. The fault slip then only produce static displacements. We invert the slip distribution on these two planes simultaneously using both seismic and geodetic data. To stable the inversion, we apply the same Laplace smoothing constraint to the slip on both fault planes but there is no "a priori" relationship between the slips in two fault planes. One site on the fault surface with large co-seismic dislocation could also have large post-seismic slip. There is also no constraint to the total seismic moment.

We have applied this approach to study the 2009 L'Aquila earthquake. Using the new source parameterization, the total number of inverted parameters increases to 1001, 40% more than the number of unknowns in Model I. The results are shown in Figure 4c ("co-seismic" slip) and Figure 5b ("post-seismic" slip). We hereafter referred them as Model III_a and III_b, respectively. As expected, the model explains the geodetic data as good as the Model II. However, the fits to the strong motion waveforms become slightly worse

than Model I. The seismic moment of Model III_a is 3.1×10^{18} Nm, yielding an Mw of 6.26. It is consistent with Model I and is mainly constrained by the long period surface waves. The slip distribution of Model III_a features two large asperities (Figure 4c). The first asperity centers at the 3 km up-dip of the hypocenter. The inverted peak slip of this asperity is 0.86m. The centroid of the second asperity is at 8 km along strike and 4 km up-dip away from the hypocenter. Most of seismic moment occurred during the failure of this asperity. Its peak slip is 0.90 m. This slip distribution is generally similar to that of Model I but it is visually much more compact. The centroid depth of Model III_a is 7.3 km, slightly deeper than Model I (7.0 km) and Model II (6.9 km). The accumulated area of subfaults with over 0.2 m slip is 142.8 km^2. The average slip within this region is 0.45 m. Figure 5d shows the moment rate function of Model III_a. The significant moment release occurred at 0.6 s after the rupture initiation and 99% of total seismic moment occurred before 10 s. We can identify three local maximums in moment rate at 2.15 s, 4.15 s and 6.50 s, with the global maximum occurring in the last.

The seismic moment of Model III_b is 0.6×10^{18} Nm, suggesting an Mw of 5.78. The accumulative seismic moment of Model III_a and III_b is 3.7×10^{18} Nm, agreeing with the Model II as what we expected. In compared with the scalar difference between Model I and II shown in Figure 5b, the slip distribution of Model III_b is much more compact. It features two separated patches as well. The centroid of first one is close to the hypocenter and that of another is located at 6 km along strike and 7 km up-dip away from the hypocenter (Figure 5a). These centroid locations are consistent with the regions with highest residuals between Model I and Model II (Figure 5b). The fact that the joint inversion results in a highly concentrated "aseismic" slip distribution seems to support that the results are at least partially realistic. It is interesting to compare Model III_b with the afterslip distribution during a half-year period since April 12, constrained by InSAR and GPS data [*D'Agostino et al.*, 2012]. The white dashed ellipses denote the regions with significant later afterslip. The seismic moment of Model III_b is compatible with the accumulative afterslip occurred during the first 60 day after April 7, 2009 (6.5×10^{17}Nm, [*Cheloni et al.*, 2010]) or during a 180-day period after April 12, 2009 ((5.1×10^{17}Nm, [*D'Agostino et al.*, 2012]). The afterslip up to 45 cm concentrates near the vicinity of the patches with high co-seismic slip. For the fault plane deeper than 4 km, the earlier afterslip occurs next to the fault paths with significant later afterslip during a 180-day period after April 12, 2009 [*D'Agostino et al.*, 2012]. For the fault plane shallower than 4 km, the fault patches with earlier and later afterslip are overlapped.

We choose Model III_a as our preferred co-seismic model as it has taken advantage of both seismic and geodetic datasets. It reveals that the energetic rupture of 2009 L'Aquila earthquake occurred 0.6 s after the rupture initiation and propagated to the up-dip direction in a speed about 2.5 km/s. This rupture produced the first pulse in moment rate function and apparently ceased at about 3-3.5 s. The accumulative seismic moment during the first 3 s is 0.5×10^{18}Nm, only 17% of the total seismic moment. Rupture then propagated along the strike at about 3.5 s to break the region connecting the two asperities, which is corresponding to the second pulse in the moment rate function. The failure of the second asperity initiated at about 4.5-5 s and continued until the end of rupture, corresponding to the last and the most dominant pulse in moment rate function.

Cirella et al. [2009] argued that the rupture propagation in the up-dip direction (~ 2.8 km/s) is significantly faster than rupture propagation in along strike direction (~ 2.0 km/s). They speculated that this feature suggests a correlation between wave speed and rupture velocity, i.e., the rupture velocity is faster in the medium with higher wave speed. As the second asperity, which is about 8 km away from the hypocenter, failed at about 4.5-5 s, our kinematic result is consistent with the result of *Cirella et al.* [2009]. However, as we described earlier, the apparently slower rupture velocity in along strike direction was more likely caused by the fault segmentation, i.e., the rupture propagation is slow down when the front encounters the boundaries of asperities.

As shown in Figure 4c, the fault area with significant slip falls in a narrow downdip distance range of 5 to 13 km. The corresponding depth range is 4-10 km. Its centroid depth of 7.4 km and the asymmetry moment rate function shown in Figure 5d confirm the previous results based on regional long period seismic data [*Herrmann et al.*, 2011], which placed the location of major moment release up-dip of the hypocenter and about 4–7 s after the rupture initiation. However, the depth distribution is inconsistent with the finite fault model of *Cirella et al.* [2009]. They also found that the fault slip occurred mainly on two asperities but their second asperity is located in a deeper depth range of 9-14 km. This discrepancy might be partially due to the difference in the fault geometry. *Cirella et al.* [2009] used a fault plane orienting N133^{o}E, in contrast with the N140^{o}E used here. As in the finite fault inversion, the horizontal location of slip is often better constrained with nearby seismic data than its vertical position, a deeper inverted slip shall be expectable as rupture propagates away in along strike direction. We notice that according to the LVZ model, the wave speed in aforementioned depth range of 4 to 10 km is abnormally high (Figure 2), suggesting a correlation between the asperity locations and high velocity anomaly. Such correlation has also been noticed during recent earthquakes, e.g., 2011 Tohoku earthquake [*Zhao et al., 2011*].

Figure 6 shows the spatial distributions of rise time and average slip velocity. The latter is defined as the ratio between the slip and rise time, which might be related with the local dynamic stress drop [*Kanamori*, 1994]. The rise time and slip velocity estimations at individual subfaults often include relatively large uncertainties, but numerical test suggested their averages weighted by slip are well constrained [*Ji et al.*, 2002]. The weighted average rise time and slip velocity estimated using Model III_a are 0.71 s and 0.77 m/s, respectively. The inverted average rise time is then considerably smaller than the previous model of *Cirella et al.* [2009]. However, this discrepancy is likely due to their "*a priori*" condition that the rise time can only change from 1.0 s to 2.0 s [*Cirella et al.*, 2009]. In particular, the rise time associating with the first asperity is only 0.4 s, the minimum value allowed during this study. Interestingly, *Cirella et al.* [2009] found that the average rise time associating with this asperity is 1.0 s, again the minimum allowed in their study. Nevertheless, it is safe to state that the fault slip of the first asperity is very energetic.

In the end, It is of interest to note that the radiated seismic energy estimated using the inverted moment rate function and the method of Vassiliou and Kanamori [1982] is 1.67 x10^{13} J. The E_s / M_o ratio is then 0.55 x10^{-5}. This is consistent with the seismic radiated

energy estimated by Dr. Choy in USGS (1.3±0.4x10^{13}J.) (http://neic.usgs.gov/neis/eq_depot/2009/eq_090406_fcaf/neic_fcaf_e.html), though his estimation was calculated entirely based on teleseismic data. The E_s / M_o ratio based on this estimation is 0.41±0.13x10^{-5}. The E_s / M_o ratio of L'Aquila earthquake is then considerably lower than either the global average (3x10^{-5}, [*Ide and Beroza*, 2001]) or the M>4.5 earthquakes in California (0.5×10^{-4} to 2×10^{-4}, [*Kanamori and Heaton*, 2000]). In contrast, for such a continental intra-plate environment, Choy and Boatwright [1995] reported that the normal fault earthquakes on average have relatively larger apparent stress drop (or E_s / M_o ratio) than the global average of shallow earthquakes. However, it is not clear yet whether it is a unique characteristic for L'Aquila mainshock or a general feature for the normal fault earthquakes in central Apennines.

Conclusions

We apply a new inversion strategy to constrain the co-seismic rupture model and earlier post-seismic afterslip model of the 2009 L'Aquila earthquake simultaneously from the joint inversion of near-source strong ground motion recordings, P teleseismic body waves, Long period Rayleigh waves, GPS displacement vectors, and InSAR line of sight (LOS) displacement image. The fault is defined to strike 140° and dip 50° to the southwest. The inverted slip history reveals that co-seismically, after a lag of 0.6 s after rupture nucleated, the rupture first propagated up-dip to break an Mw 5.7 asperity and then propagated along strike to break a large patch located 8 km along strike and 4 km up-dip from the hypocenter. Our estimate of co-seismic scalar moment is 3.1 X 10^{18} Nm, 99% occurred in the first 10 s. The average slip during this period is 0.4 or 0.45 m, dependent of the average strategies. The peak slip reaches about 0.90 m. Most co-seismic slip occurs in a small rupture area of approximately 16 km along strike and nearly 8 km in the dip direction, in a depth range of 4-10 km. The weighted average rise time and slip velocity are 0.71 s and 0.77 m/s, respectively. The initial up-dip rupture has a rupture velocity about 2.5 km/s, 65% of local S-wave speed. The propagation along the strike is slower on average, apparently caused by fault segmentation. Our estimate of radiated seismic energy is 1.67 x10^{13} J., yielding an energy moment ratio of 0.55 x10^{-5}, significantly small than the global average of shallow earthquake [*Ide and Beroza*, 2001].

The earlier post-seismic period here mainly represents the time window from 10 s to the first day, which might be contaminated by the post-seismic deformation occurred April 7, 2009 to April 12, 2009. Our result suggests that the accumulative afterslip during this period is 6.0x10^{17} Nm, equivalent to an Mw of 5.8. It is roughly same as the accumulative afterslip occurred during the first 60 day after April 7, 2009 (6.5x10^{17}Nm, [*Cheloni et al.*, 2010]) or during a 180-day period after April 12, 2009 ((5.1x10^{17}Nm, [*D'Agostino et al.*, 2012]). The afterslip up to 45 cm concentrates near the vicinity of the patches with high co-seismic slip. For the fault plane deeper than 4 km, the earlier afterslip occurs next to or partially overlaps with the fault paths with significant later afterslip during a 180-day period after April 12, 2009 [*D'Agostino et al.*, 2012]. For the fault plane shallower than 4 km, the fault patches with earlier and later afterslip are overlapped. This result reflects that the fault patches with large post-seismic slip have

individual decay rates, which spans a broaden range from as short as hours (this study) to a few months in a term of the decay constant [*D'Agostino et al.*, 2012].

Figures

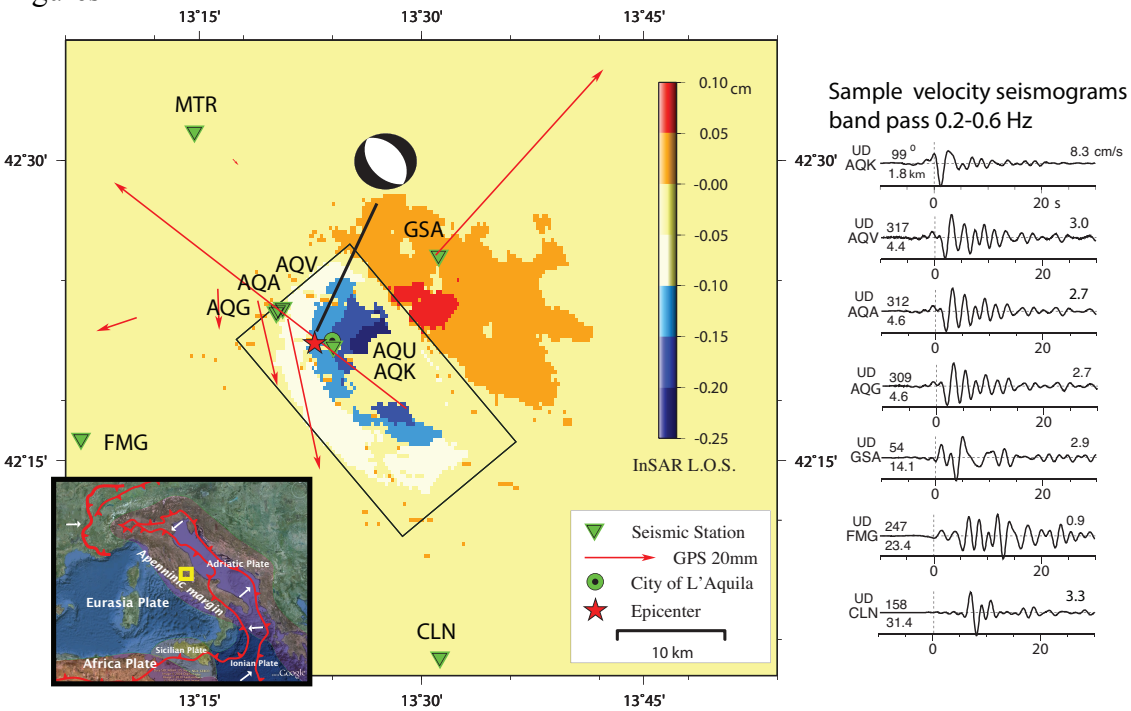

Figure 1. Near-source observations of the 2009 L'Aquila earthquake. The color denotes the LOS displacement. Red arrows denote the horizontal displacements. The triangles show the strong motion stations. The vertical components of bandpassed velocity seismograms are shown in the left. The low-inset denotes the tectonic setting.

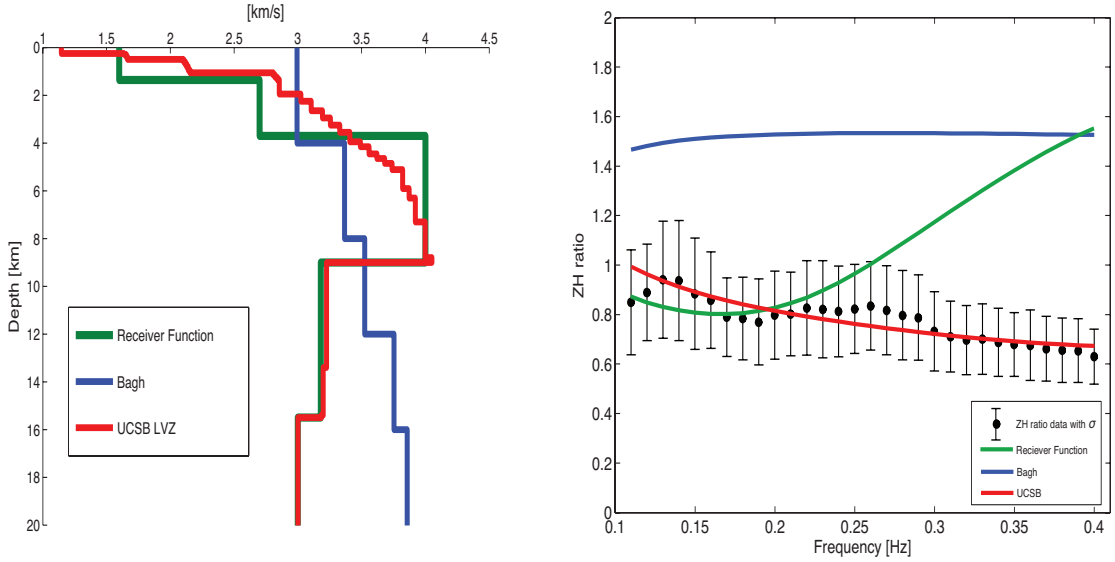

Figure 2. Left: comparison of velocity models. Right: Comparison of observed ZH ratios with synthetics calculated using three different velocity models.

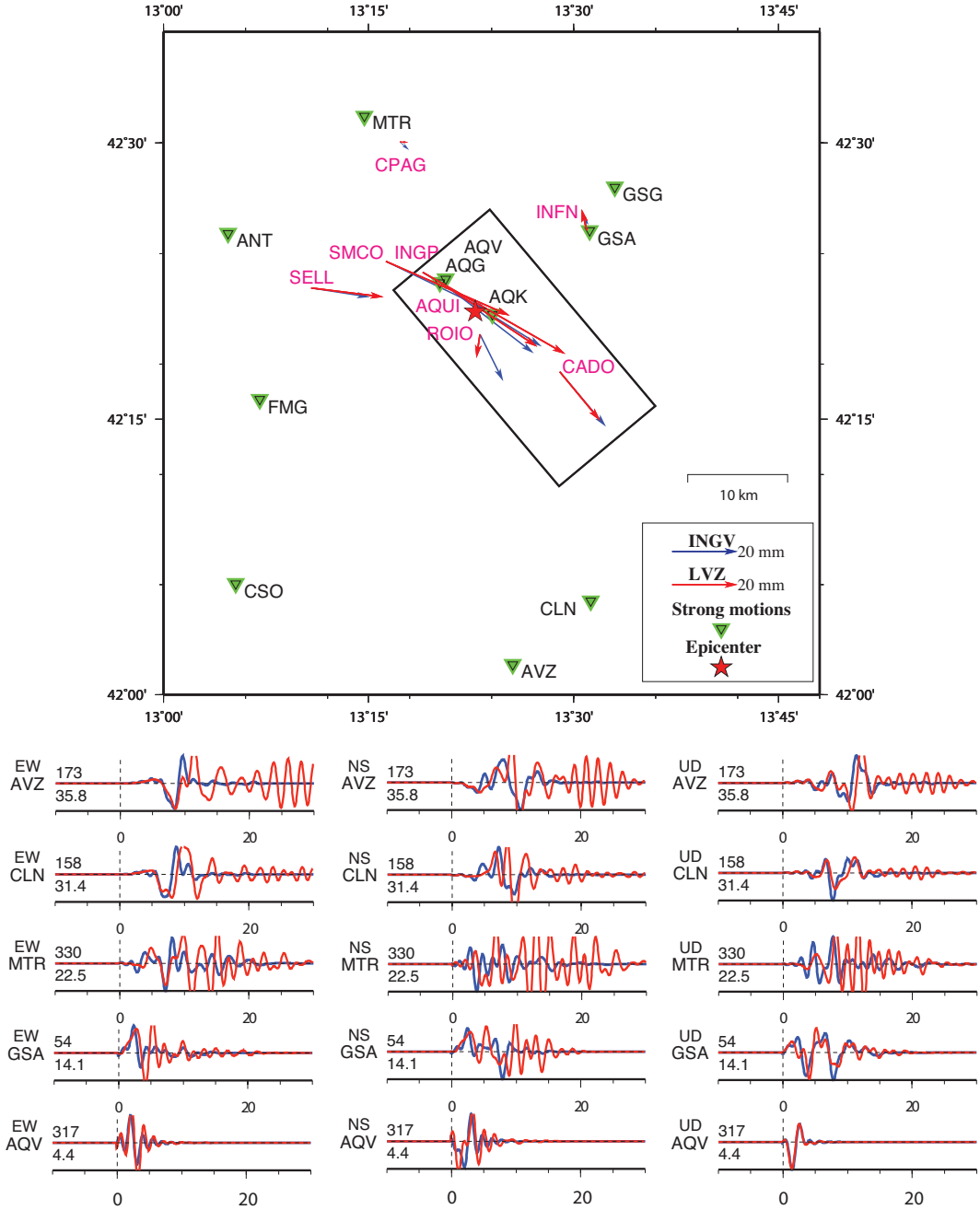

Figure 3. Effects of velocity structures. The red and blue vectors and lines denote static horizontal displacements and velocity waveforms of 1-point source at the hypocenter, using Bagh and LVZ models, respectively.

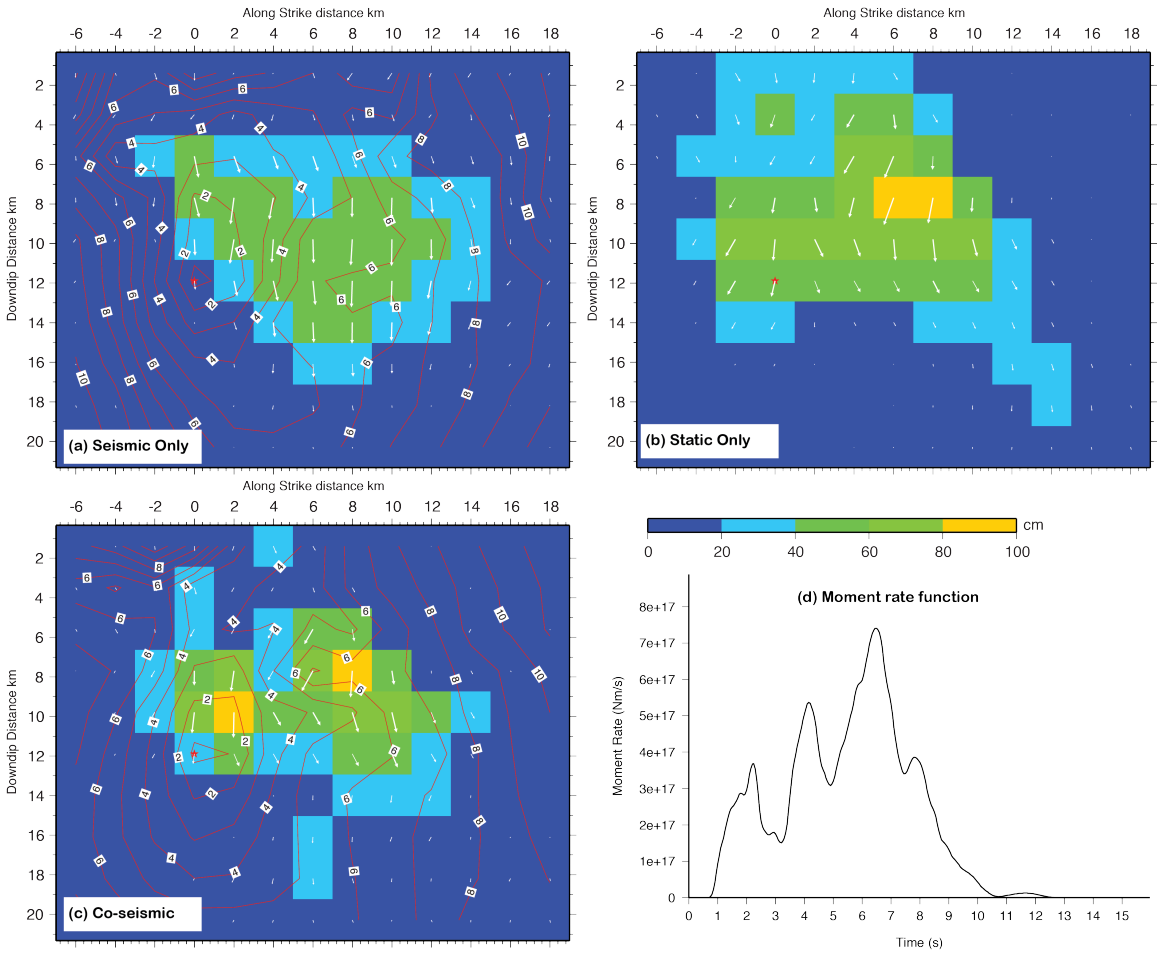

Figure 4. Comparison of slip models. (a) Model I, constrained using strong motion, teleseismic body waves, and surface waves. (b) Model II, constrained using GPS vectors and INSAR LOS displacements. (c) Model III, the preferred coseismic slip distribution by joint inverting the seismic and geodetic data. (d) The moment rate function based on the preferred slip model.

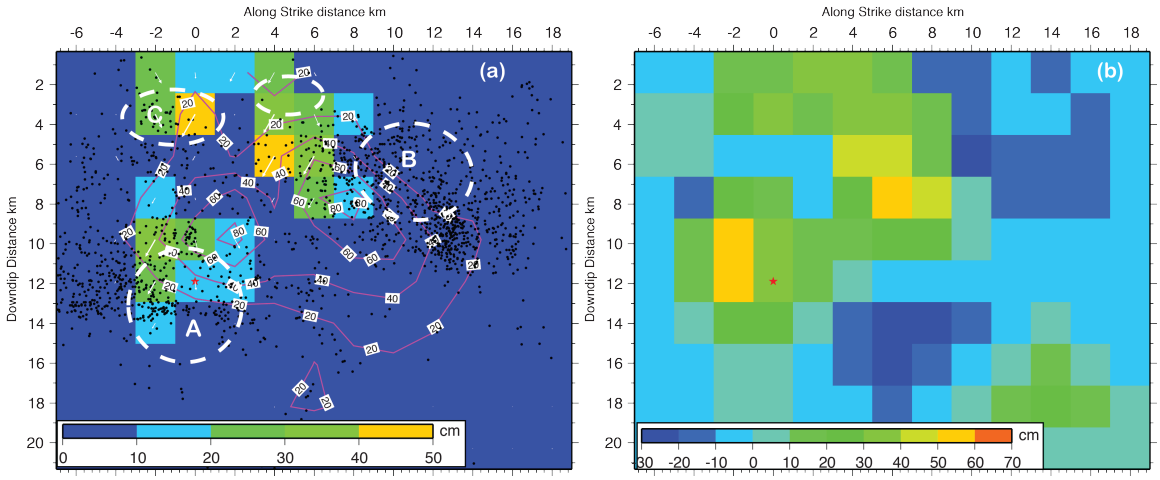

Figure 5. (a) The earlier afterslip model (Model III_b) constrained using both seismic and geodetic data. The pink contours denote the slip distribution of Model III_a and white dashed ellipses show the locations with significant cumulative afterslip during first 6 months since April 12, 2009, six days after the 2009 L'Aquila earthquake. The black dots denote the aftershocks. (b) For a comparison, scalar difference between Model II and Model I.

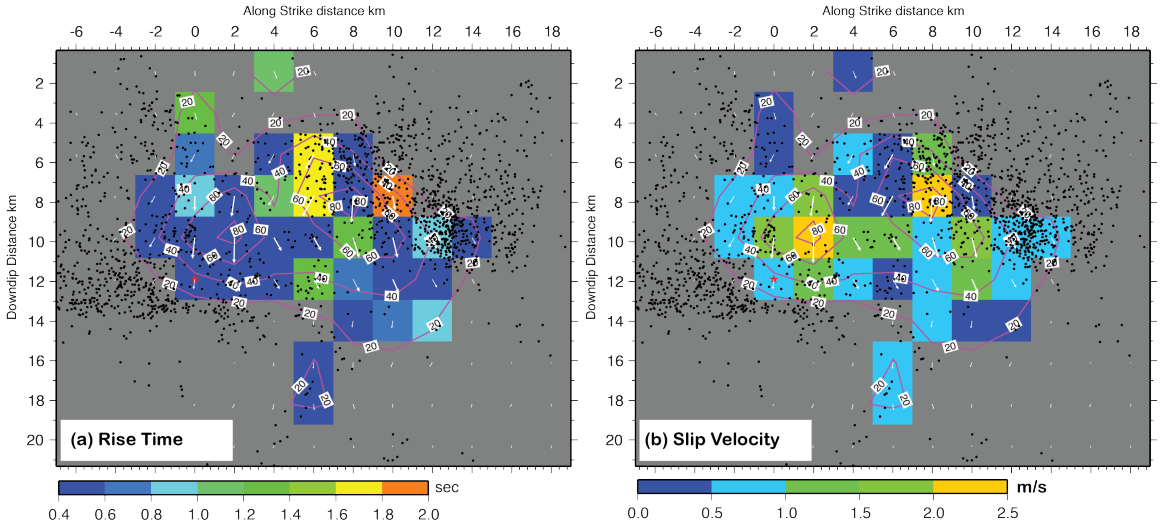

Figure 6 (a) distribution of rise time. (b) distribution of average slip velocity. Only the subfaults with slip larger than 0.2 m are used. The black dots denote the aftershocks. The contours show the slip distribution in cm.

Meeting abstracts

[*Yano et al*., 2009] *2009 AGU Fall meeting S34A-02*

Finite Fault Kinematic Rupture Model of the 2009 Mw6.3 L'Aquila Earthquake from Inversion of Strong Motion, GPS and InSAR Data

The Mw6.3 L'Aquila earthquake of April 6, 2009 is the M>6 normal faulting earthquake with the best near-source strong motion observations. Seventeen strong motion accelerographs are within 50km of the surface projection of the fault plane. Of these ten are within 20 km, and four of them are right above the fault plane. The data coverage is further improved with additional GPS and InSAR, providing an excellent opportunity to investigate the detailed rupture process of a normal-faulting earthquake. The L'Aquila earthquake sequence also includes more than 20 well-recorded aftershocks with magnitude 4.0 or higher, which could be used to modify the velocity model and/or account for local site amplification. We use two independent nonlinear inversion methods (Ji et al., 2002 and Liu and Archuleta, 2004) to constrain the kinematic rupture history. Our preliminary slip model based on the 3-component records of 17 strong motion stations adopts a fault plane with a strike of 142 and a dip of 48 degrees to the southwest. In this model the rupture initiates at a depth of 8.3 km and then primarily propagates updip and to southeast for over 20 km with an average velocity of 1.6-1.8 km/s along strike and about 2.1 km/s updip. The inverted slip distribution shows almost pure normal faulting although the rupture to the northwest is small and oblique. The model produces a seismic moment of 3.44 X 10**18 Nm. The inverted peak slip is 80 cm, occurring about 8 km southeast of the hypocenter. Synthetics match the data generally well, except for stations right above the fault plane. For these stations, the vertical amplitude and phase are well fit, but the horizontal amplitudes are less than half of the observed even though their phases are in good agreement. The InSAR data and the GPS data could provide additional information, and will be included to constrain the future inversions. We will present the solution based on all of these data at the meeting.

[*T. E. Yano et al.*, 2010a] *2010 SCEC Annual Meeting poster 2-063*

Finite Fault Co-seismic Kinematic and Post-Seismic Slip Distribution Model of the 2009 Mw 6.3 L'Aquila Earthquake from Joint Inversion of Strong Motion, GPS, and InSAR Data

April 6, 2009 Mw6.3 L'Aquila earthquake occurred in the central Apennines near the medieval town, L'Aquila. The L'Aquila area has been known as one of high seismic risk locations. Historical earthquakes affecting L'Aquila occurred in 1461, 1762, 1916, and 1958 (Rossi et al., 2005).

For near-source strong motion observations of normal faulting the 2009 has the best data set. Seventeen strong motion accelerographs are within 50km of the surface projection of the fault plane. Of these 10 are within 20 km, and five are above the fault plane. The highest accelerations occur for these five stations on the hanging wall with peak horizontal accelerations in the range of 347- 662 cm/s2 and peak velocities in the range of 32-42 cm/s. To understand the earthquake process, we have used the nonlinear inversion method of Ji et al. (2002) to jointly invert the strong motion data and static field measurements, such as GPS and InSAR, for two models: a co-seismic kinematic model and a post-seismic slip distribution. Based on several different inversions we settled on a fault with a dip of 50 degrees to the southwest. We use a strike of 140 degrees which is consistent with the InSAR and with the limited lineament of surface breakage.

In our co-seismic model, the rupture initiates at a depth of 9.1 km and then primarily propagates updip and to southeast for more than 20 km with an average velocity of 2.0 km/s along strike and updip. The maximum slip, about 70 cm, occurs in two locations: one near the hypocenter and the other about 6 km southeast of hypocenter. The co-seismic moment is 2.9 x 10**18 Nm. In our post-seismic model, 40 cm slip appears updip from the hypocenter. The seismic moment of the post-seismic model is 1.2 x 10**18 Nm, about 40 % of the co-seismic moment.

[*T. E. Yano et al.*, 2010] *ESD 2010* on page 63

CO- AND POST-SEISMIC KINEMATIC MODEL FOR THE APRIL 6 2009 MW 6.3 L'AQUILA EARTHQUAKE BY INVERSION OF THE STRONG MOTION, GPS, AND INSAR DATA

Mw 6.3 L'Aquila earthquake is the best-recorded normal-faulting event in near-source strong motion observations. 17 strong motion accelerographs are within 50 km of the surface projection of the fault plane. Of these 10 are within 20 km, and 4 are above the fault plane. In addition to the strong motion observations there are static measurements including GPS and InSAR. Having both seismic and static recordings provides excellent coverage of faulting for the mainshock and aftershocks.

We use strong motion records and static field measurements to invert simultaneously for two models: a co-seismic kinematic model and a postseismic slip distribution. We introduced this approach because the static field records include deformation that occurred several days following the mainshock. The co-seismic model describes the rupture process, which can explain both seismic and static data. The post-seismic model shows the slip on the fault that cannot be explained by the seismic data.

The fault has a dip of 55 degrees to the southwest constrained by the aftershock hypocenter locations given by Chiaraluce at INGV. In our coseismic model, the rupture initiates at a depth of 9.2 km and then primarily propagates updip and to southeast for over 20 km with an average velocity of 2.0 km/s along strike and about 2.0 km/s updip. The maximum slip is about 80 cm in two locations, one near the hypocenter and the other about 6-8 km southeast of hypocenter. The co-seismic moment is 3.2 x 1018 Nm. In our post-seismic model, 40 cm slip appears above the hypocenter and 20 cm slip around the hypocenter. The post-seismic model has a moment of 7.8 x 1017 Nm.

We will present this approach that inverts for co-seismic and post-seismic model based on all of the data.

[*T. E. Yano et al.*, 2010b] *Seismological Research Letters* Volume 81, No. 2 on page 365

FINITE FAULT KINEMATIC RUPTURE MODEL OF THE 2009 MW 6.3 L'AQUILA EARTHQUAKE FROM JOINT-INVERSION OF STRONG MOTION, GPS AND INSAR DATA

The 6 April 2009 Mw 6.3 L'Aquila earthquake is the best-recorded normal faulting event for near-fault strong motion and static field measurements. The highest accelerations occur for five stations on the hanging wall directly above the fault with peak horizontal accelerations in the range of 347- 662 cm/s^2 and peak velocities in the range of 32-42 cm/s. To understand what led to the distribution of ground motions, we have jointly inverted the strong motion data and static field data. We used 14 strong motion accelerograms within 50 km. The accelerograms are integrated to velocity with a passband of 0.2 – 0.6 Hz. We have used both GPS and InSAR data to constrain the static field. In our initial model we assume a single, planar fault that has a strike of 140˚ and a dip of 45˚. We use nonlinear inversion method (Ji et al., 2002) to constrain the kinematic rupture history. First, we inverted each data set separately. In the static only inversion the maximum slip is about 100 cm with some slip located near the surface. For seismic only inversion the maximum slip is about 80 cm with no slip at the surface. The joint-inversion produces maximum slip about 100 cm in a patch that is about 6 km southeast of the hypocenter, and some slip located near the surface. The rupture propagation is primarily updip and to the southeast. The rupture velocity is relatively slow, about 2 km/s. These preliminary models will be re-examined to determine if the fit between the data and synthetics can be improved. We will also use isochrones to check for consistency between the synthetics and the arrival of phases at frequencies higher than we can resolve in the inversion.

Reference

Bagh, S., L. Chiaraluce, P. De Gori, M. Moretti, A. Govoni, C. Chiarabba, P. Di Bartolomeo, and M. Romanelli (2007), Background seismicity in the central Apennines of italy: The Abruzzo region case study, *Tectonophysics*, *444*(1-4), 80-92.

Cheloni, D., et al. (2010), Coseismic and initial post-seismic slip of the 2009 M(w) 6.3 L'Aquila earthquake, Italy, from GPS measurements, *Geophys. J. Int.*, *181*(3), 1539-1546.

Choy, G. L., and J. L. Boatwright (1995), GLOBAL PATTERNS OF RADIATED SEISMIC ENERGY AND APPARENT STRESS, *J. Geophys. Res.-Solid Earth*, *100*(B9), 18205-18228.

Cirella, A., A. Piatanesi, M. Cocco, E. Tinti, L. Scognamiglio, A. Michelini, A. Lomax, and E. Boschi (2009), Rupture history of the 2009 L'Aquila (Italy) earthquake from non-linear joint inversion of strong motion and GPS data, *Geophys. Res. Lett.*, *36*.

D'Agostino, N., D. Cheloni, G. Fornaro, R. Giuliani, and D. Reale (2012), Space-time distribution of afterslip following the 2009 L'Aquila earthquake, *J. Geophys. Res.-Solid Earth*, *117*.

Herrmann, R. B., L. Malagnini, and I. Munafo (2011), Regional Moment Tensors of the 2009 L'Aquila Earthquake Sequence, *Bull. Seismol. Soc. Amer.*, *101*(3), 975-993.

Ide, S., and G. C. Beroza (2001), Does apparent stress vary with earthquake size?, *Geophys. Res. Lett.*, *28*(17), 3349-3352.

Ji, C., D. J. Wald, and D. V. Helmberger (2002), Source description of the 1999 Hector Mine, California, earthquake, part I: Wavelet domain inversion theory and resolution analysis, *Bull. Seismol. Soc. Amer.*, *92*(4), 1192-1207.

Kanamori, H. (1994), Mechanics of Earthquakes, *Annu. Rev. Earth Planet. Sci.*, *22*, 207-237.

Kanamori, H., and T. Heaton (2000), Microscopic and macroscopic physics of earthquakes, in *GeoComplexity and the Physics of Earthquakes, Geophys. Monogr. Ser.*, edited by J. B. Rundle, D. L. Turcotte and W. Klein, pp. 147-163, American Geophysical Union, Washington, D. C.

Romanowicz, B., and P. Guillemant (1984), An Experiment in the Retrieval of Depth and Source Mechanism of Large Earthquakes Using Very Long-Period Rayleigh-Wave Data, *Bull. Seismol. Soc. Amer.*, *74*(2), 417-437.

Rosen, P. A., G. Hensley, G. Peltzer, and M. Simons (2004), Updated Repeat Orbit Interferometry package released, *Eos Trans. AGU*(85), 35.

Simons, M., Y. Fialko, and L. Rivera (2002), Coseismic deformation from the 1999 M-w 7.1 Hector Mine, California, earthquake as inferred from InSAR and GPS observations, *Bull. Seismol. Soc. Amer.*, *92*(4), 1390-1402.

Vassiliou, M. S., and H. Kanamori (1982), The Energy-Release in Earthquakes, *Bull. Seismol. Soc. Amer.*, *72*(2), 371-387.

Yano, T., T. Tanimoto, and L. Rivera (2009), The ZH ratio method for long-period seismic data: inversion for S-wave velocity structure, *Geophys J Int*, *179*(1), 413-424.

Yano, T. E., G. Shao, Q. Liu, C. Ji, and R. J. Archuleta (2009), Finite Fault Kinematic Rupture Model of the 2009 Mw6.3 L'Aquila Earthquake from Inversion of Strong Motion, GPS and InSAR Data, *(2009 AGU Fall meeting oral)*.

Yano, T. E., G. Shao, Q. Liu, C. Ji, and R. J. Archuleta (2010a), Finite Fault Co-Seismic Kinematic and Post-Seismic Slip Distribution Model of the 2009 Mw 6.3 L'Aquila Earthquake from Joint-Inversion of Strong Motion, GPS, and InSAR Data, *(2010 SCEC Annual Meeting poster)*.
Yano, T. E., G. Shao, Q. Liu, C. Ji, and R. J. Archuleta (2010), Co- and Post-Seismic Kinematic Model for the April 6 2009 Mw 6.3 L'Aquila Earthquake by Inversion of the Strong Motion, GPS, and InSAR Data, *(2010 ESD Smolenice Castle, Slovak Republic oral)*.
Yano, T. E., G. Shao, Q. Liu, C. Ji, and R. J. Archuleta (2010b), Finite Fault Kinematic Rupture Model of the 2009 Mw 6.3 L'Aquila Earthquake from Joint-Inversion of Strong Motion, GPS and InSAR Data, *(2010 SSA Annual Meeting oral)*.